Variability in shortwave irradiance caused by forest gaps: Measurements, modelling, and implications for snow energetics

Keith N. Musselman [a,*], John W. Pomeroy [a], Timothy E. Link [b]

[a] University of Saskatchewan, Centre for Hydrology, 117 Science Place, Saskatoon, Saskatchewan S7N 5C8, Canada
[b] College of Natural Resources, University of Idaho, 875 Perimeter Drive MS 1133, Moscow, Russia

ARTICLE INFO

ABSTRACT

Solar irradiance in and around forest gaps plays a key role in determining the snowmelt patterns that shape how forest gaps influence spring snow cover retention relative to open or continuously forested landscapes. To reduce uncertainty in forest gap snowmelt estimation, a new canopy solar transmittance model was developed to include the effects of shading and enhanced transmittance. The model couples a new a ray tracing approach with an existing canopy solar radiation extinction and transmission model. The new model analytically solves for the path length of a solar ray (beam) through a forest canopy and potential intersection(s) with a forest gap conceptualized as an upright circular cylinder surrounded by homogeneous forest. The model was tested alongside simpler transmittance models that ignored shading and treated the canopy as either a binary (open or forested) classification or that used proximal canopy descriptors. The models were evaluated using measurements of shortwave radiation from 20 pyranometers in and around a 56 m diameter gap in a coniferous forest. Errors from ignoring shading were greatest in the gap near the forest edge and in the forest nearest the northern gap edge. The new model reduced these errors; at the 20 pyranometer locations, individual biases up to +356 W m^{-2} and average biases up to +101 W m^{-2} were reduced to better than ±5 W m^{-2}. Results suggest that an accurate description of spatial variability of solar irradiance in and around a forest gap requires explicit treatment of the effects of shading into a gap and enhanced transmittance beyond the gap extent; this is dependent upon solar position, gap and forest geometry, and location relative to the gap. A sensitivity experiment with the forest gap – ray trace model in which gap size, latitude, and day of year were varied under clear-sky conditions showed that cumulative daily solar irradiance has high spatiotemporal variability. The maximum of the spatial coefficient of variation (CV) of cumulative daily irradiance was a function of gap size and solar angles; smaller (larger) gaps and lower (higher) solar elevation angle ranges were more diffuse- (direct beam-) dominated with reduced (increased) spatial variability relative to the mean. It is found that there is no standard impact of a forest gap on shortwave irradiance – the impact of gap size on clear sky solar irradiance depends on forest structure, date, and latitude.

© 2015 Elsevier B.V. All rights reserved.

1. Introduction

Solar radiation is a principal driver of ecological processes including net primary productivity (Monteith, 1972) and forest species composition (Clark and Clark, 1992; Denslow, 1980; Nicotra et al., 1999) and hydrological processes such as soil moisture (Western et al., 1999) and snowmelt (Male and Gray, 1981; Marks et al., 1992; Pomeroy et al., 1998). Estimating the magnitude and variation of shortwave radiation is therefore of paramount importance in many ecological and hydrological applications; this is particularly difficult in discontinuous forested environments characterized by gaps and small clearings (Baldocchi and Collineau, 1994; Canham, 1988; Gray and Spies, 1996; Gray et al., 2002; Runkle, 1981; Spies and Franklin, 1989). Compared to full sun conditions, continuous forest canopy coverage reduces the magnitude of solar radiation incident on the forest floor (Anderson, 1964; Miller, 1959). Uniform canopy cover also limits the spatial variability compared to that observed beneath sparse or heterogeneous forests (Pomeroy et al., 2008; Reifsnyder et al., 1971). The assumption of horizontal canopy homogeneity facilitates the numerical estimation of solar transmittance with a widely-used probabilistic application (Monsi and Saeki, 1953) of the Beer–Lambert law; however, typical forest structure is highly non-uniform. Particularly, canopy disconti-

nuities in the form of small gaps and clearings invalidate the underlying assumptions of the Beer–Lambert law.

Numerous canopy solar radiation transfer models account for the effect of forest structure heterogeneities in a probabilistic manner with trunks and crowns abstracted by geometric shapes (e.g., Ellis and Pomeroy, 2007; Ni et al., 1999, 1997; Nijssen and Lettenmaier, 1999; Satterlund, 1983; Seyednasrollah et al., 2013). These sophisticated models have many parameters that require extensive field observation and careful calibration on sub-canopy radiation measurements. Even fewer models explicitly resolve the spatial patterns of solar transmittance in and around individual canopy discontinuities or 'gaps'. The light environment of a forest gap exhibits dynamic patterns caused by solar angles, gap size and shape, cloudiness, and forest stand characteristics (Canham, 1988; Canham et al., 1990; Ellis et al., 2013; Golding and Swanson, 1978; Lawler and Link, 2011). To account for these complex sub-canopy light patterns, models generally represent gap geometry in a conceptual manner as an upright cylindrical opening surrounded by forest canopy (e.g., Canham, 1988; Lawler and Link, 2011; Seyednasrollah and Kumar, 2014) and scale the canopy transmittance of diffuse and direct radiation according to the sky view and the canopy path length, respectively.

The ability to characterize shortwave radiation at high spatial resolution in discontinuous forest environments is attractive for a number of reasons. First, it serves to advance the understanding of global forest–water–climate interactions. For example, studies of seasonal snow dynamics often compare observations and/or model results obtained from a canopy gap or forest clearing to those from uniformly forested areas (e.g., Lundquist et al., 2013 and references therein). While there may be logistical and methodological reasons for making such comparisons, it is imprecise to abstract forests as a binary sequence of gaps and non-gaps (Lieberman et al., 1989). This bulk approach neglects canopy edge effects and subsequent microclimatological gradients that dictate spatiotemporal patterns of net radiation, sensible and latent heat fluxes, land surface temperature and water availability. Second, spatially explicit characterization of the surface energy budget in heterogeneous forests could inform the representativeness of hydrological and ecological monitoring sites that are often located in small forest gaps to the surrounding environment (Meromy et al., 2013). Third, the spatial distribution of melt energy to snow has been shown to have an important influence on snow-cover depletion curves and sub-grid variability in snowmelt energetics and meltwater runoff synthesis (Essery and Pomeroy, 2004; Essery et al., 2003; Faria et al., 2000). Fourth, there is a pressing need for improved understanding of the ecological and hydrometeorological impacts of emerging forest disturbances such as the development of oil and gas wells across much of the forested landscape in Alberta, Canada (MacFarlane, 1999; Northrup and Wittemyer, 2013; Pickell et al., 2013). Likewise there is need to understand the fine-scale spatiotemporal variations in radiative fluxes resulting from forest manipulation practices designed to enhance snow retention (e.g., Berry and Rothwell, 1992; Golding and Swanson, 1986; Troendle, 1983) and to create shaded fuel breaks for fire behavior modification (e.g., Agee et al., 2000; Finney, 2001). Finally, fine-scale energy balance modelling in complex vegetated areas can be used to evaluate ecohydrological scale dependencies in the spatial correlations among vegetation distribution, water availability (e.g., canopy interception, snowmelt rates, evapotranspiration), and the surface energy budget (Thompson et al., 2011).

Toward this end, field-validated model simulations of spatiotemporal solar irradiance patterns in and around forest gaps can inform how the influence of gaps on the sub-canopy light and energy environment varies seasonally, with latitude, and with gap structure. For example, Canham (1988) and Canham et al. (1990) developed a sophisticated model of photosynthetically active irradiance (PAR; 380–710 nm) in and around conceptualized cylindrical forest gaps for a range of low to mid-latitudes (10–44°N), slopes, aspects, and tree species. The studies reported the relative magnitude of PAR averaged over the growing season at locations in and around relatively small gaps (75–100 m^2) to that expected beneath a continuous forest canopy. Details of the direct beam canopy transmittance model were not published, challenging efforts to extend the model from the intended ecological application to snow hydrometeorological applications that include more northerly latitudes, different times of year, larger canopy gaps, different gap shapes, and a broader range of solar energy wavelengths (e.g., 305–2800 nm). More recently, Lawler and Link (2011) developed a field-verified model to estimate the net shortwave and longwave radiation along a linear transect bisecting a circular forest gap. The authors used the canopy path length, determined analytically from gap position, size, and solar angles, to scale the shortwave direct beam canopy transmittance; however, the path length calculation was not extended to a gridded configuration necessary to predict spatial irradiance patterns.

There is much need to enhance the understanding of the spatiotemporal shortwave radiation dynamics in discontinuous forests through modelling underpinned by detailed measurements. To accomplish this general goal, the following specific objectives were addressed:

1. Document the spatiotemporal differences in shortwave irradiance between discrete sensor locations along a transect bisecting an approximately circular canopy gap,
2. Evaluate the ability of a new spatially explicit conceptual canopy gap solar transmittance model, forced with above-canopy radiation measurements, to simulate observations made in and around the canopy gap,
3. Examine potential differences between this conceptual, but physically based canopy transmittance model and (i) a binary gap – forest model and (ii) a model parameterized with a proximal sky view metric, and
4. Assess the sensitivity of the effects of gap size, latitude, and time of year on the modelled (clear-sky) solar irradiance patterns in and around conceptualized circular forest gaps.

Such an approach can extend existing knowledge on irradiance in and around forest gaps to seasons with snow cover (i.e., winter and spring), a broader range of the solar energy spectrum (e.g., 305–2800 nm) and more northerly latitudes (i.e., >44°N), including a large fraction of North American coniferous forest.

2. Methods

2.1. Solar radiation models

A general solar radiation canopy transmittance model is first presented followed by three variations on the treatment of the direct beam canopy transmittance: a simple model that ignores shading, a model of intermediate complexity that scales beam transmittance according to proximal gap fraction, and a more complex model that analytically solves for the beam path length through a discontinuous canopy. In the general model, downward global shortwave radiation ($SW_\downarrow$) (W m^{-2}) measured at the sub-canopy surface, hereafter referred to as solar irradiance, is defined as:

$$SW_\downarrow = SW_{0\downarrow dir}\tau_{dir} + SW_{0\downarrow dif}\tau_{dif} \qquad (1)$$

where $SW_{0\downarrow dir}$ and $SW_{0\downarrow dif}$(W m^{-2}) are the direct and diffuse components of the above-canopy global incoming shortwave radiation ($SW_{0\downarrow} = SW_{0\downarrow dir} + SW_{0\downarrow dif}$), and τ_{dir} and τ_{dif} represent the canopy
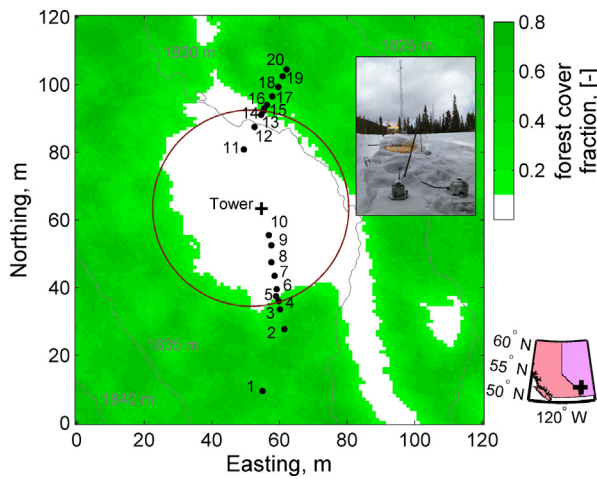
Fig. 1. The forest gap experiment site in Marmot Creek Research Basin, Alberta, Canada. Locations of 20 pyranometers (filled circle symbols) transecting the gap in a N–S orientation are indicated. The 15 m meteorological tower (center of gap) used to measure above-canopy solar radiation is shown ('+' symbol). LiDAR-derived forest cover fraction and 5 m elevation contour lines illustrate the general shape of the gap and the relatively flat (slopes <5%) topography, respectively. A circle (28 m radius; approximately centred on the gap) used to conceptualize the geometry of this forest gap is plotted. The deforested strip in the lower right is an old access road. The photo of the site is viewed from Sensor 5 northward toward the 15 m reference tower at the center of the gap.

transmittance of the direct and diffuse components, respectively. and were partitioned from measurements of $SW_{0\downarrow}$ as an empirical function of atmospheric transmissivity using the all-sky solar partition model presented in Allen et al. (2006). The canopy transmittance of the diffuse component is estimated as:

$$\tau_{\text{dif}} = \nu \qquad (2)$$

where ν is the sky view factor commonly measured at a point from a digital hemispherical photo or modelled over a spatial domain using 3-D geographic information (e.g., Rich et al., 1994). The direct beam transmittance at time t is defined as in Pomeroy and Dion (1996) as:

$$\tau_{\text{dir}_t} = e^{-\mu_t \ell_t} \qquad (3)$$

where μ_t is the extinction coefficient and ℓ_t is the path length (m) of the solar beam transmission through a homogeneous forest canopy. The path length at time t is defined as a function of the time-variant solar angle θ_t (radians) and the vertical depth of scattering elements (m) as:

$$\ell_t = \frac{h}{\sin(\theta_t)} \qquad (4)$$

The solar coordinates were computed as in Reda and Andreas (2004) at five-minute time steps for daylight hours (i.e., $SW_{\downarrow 0_t} > 0$). The extinction coefficient is defined as in Pomeroy and Dion (1996) as:

$$\mu_t = Q_t \frac{L'}{h} \qquad (5)$$

where is the effective plant area index (m² m⁻²) inclusive of needle clumping effects i.e., $L' = \text{LAI}\Omega$, LAI is the actual leaf area per unit ground area and Ω is the clumping index (Gower and Norman, 1991; Smith et al., 1993). The extinction efficiency Q_t in Eq. (5) is a time-variant function of solar angle θ_t and is formulated as in Pomeroy et al. (2009) as:

$$Q_t = \xi \theta_t \cos(\theta_t) \qquad (6)$$

The empirical coefficient ξ was determined for the montane Engelmann spruce forest of Marmot Creek (L' value of 2.95) by
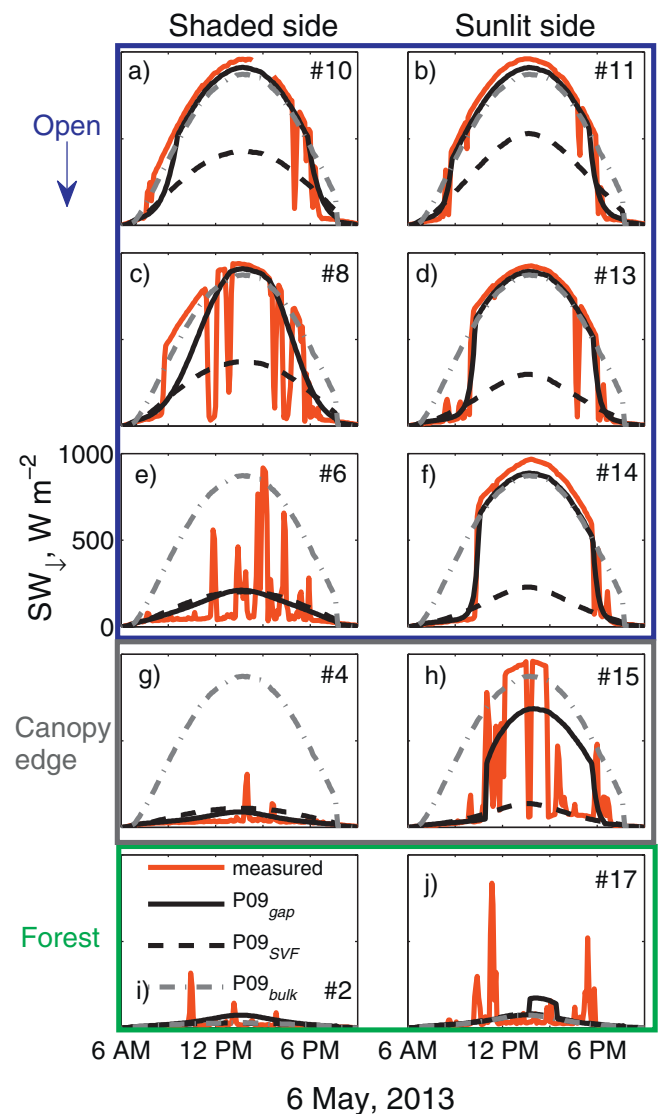

Fig. 2. Shortwave radiation at the snow surface on May 6, 2013 at select locations in and around a forest gap as measured (red line) and modelled with the geometric gap model ($P09_{gap}$; black solid line), the sky-view model ($P09_{svf}$; black dashed line), and the binary-tiled classification ($P09_{bulk}$; gray dashed line). Panels (a) through (j) represent different sensor locations. Sensor numbers at right of right of each panel correspond to those in Fig. 1. The left and right columns correspond to the south (shaded) and north (sunlit) sensor transects, respectively. Panels are ordered from the open (top panels a–f grouped within the blue box) to the canopy edge (middle panels g–h grouped within the gray box) to well within the forest (bottom panels i–j grouped within the green box). (For interpretation of the references to color in this figure legend, the reader is referred to the web version of this article.)

calibration on shortwave measurements to be 1.34; higher than the 1.081 reported from a boreal jack pine stand study (Pomeroy et al., 2009). While numerous publications contributed to the development of the shortwave canopy transmittance model described above, for ease of reference it is here referred to as the Pomeroy et al. (2009) or '*P09*' model. Note that the model does not explicitly account for the reflection or multiple scattering of direct or diffuse radiation incident on the ground surface or canopy elements, but does so implicitly through the value of the empirical coefficients developed from transmittance measurements when the sub-canopy surface was snow-covered and highly reflective. As noted previously, solar irradiance in and around a forest gap was modeled using the general *P09* model with three variations on the treatment of the direct beam transmittance. The first model tested is an example of tiled land surface schemes in that a binary (tiled),
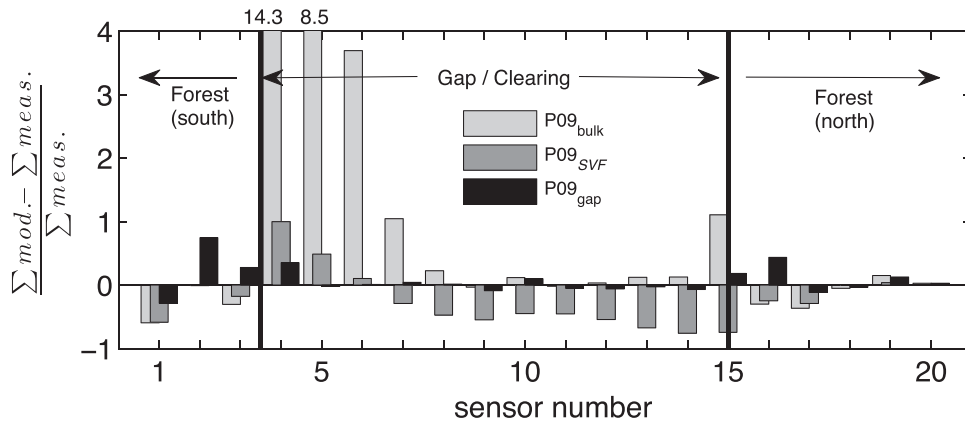
Fig. 3. Normalized cumulative error in modeled shortwave radiation on May 6, 2013 along the 20-sensor transect traversing the approximately N–S oriented forest-gap-forest transect. Note that error values for the $P09_{bulk}$ model at sensors 4 and 5 exceed the range of the y-axis at 14.3 and 8.5, respectively. The approximate locations of the gap/forest edges relative to the sensor transect are indicated by the vertical lines. The x-axis is not to scale; see Fig. 1 for spatial reference.

aggregated or 'bulk' treatment (i.e., $P09_{bulk}$) of the forest canopy that considers the forest to be a homogeneous medium with constant $L' = 2.95$ and the gap to be an open area uninfluenced by the surrounding forest. If there is forest cover directly overhead, then the direct beam is treated as in Eq. (3). In the gap, $\tau_{dir} = 1$ for all time periods. This binary tiled model deliberately ignores the shadow cast by forest edges into, and enhanced transmittance beyond the extent of, a vertically projected gap outline; $P09_{bulk}$ thus serves as a baseline model to highlight the importance of representing variable solar transmittance in and around canopy gaps.

The second model tested varied direct beam transmittance only according to the sky view, v, either measured by hemispherical photo at a point or estimated geometrically based on position within an idealized cylindrical canopy gap with a specified radius and forest height as in Essery et al. (2008). The sky view transmittance model is referred to as $P09_{SVF}$. It allows for a spatially distributed calculation of irradiance patterns in and around canopy gaps and is an advance on the binary tiled calculation of $P09_{bulk}$. A best-fit empirical relationship between L' and v as determined from optical measurements in eight conifer forest stands across western Canada by Pomeroy et al. (2009) was used to scale the direct beam transmittance in Eqs. (3) and (5) based on v values as

$$L' = e^{-(v-0.45)/0.29} \tag{7}$$

Like $P09_{bulk}$, however, the sky view factor approach lacks directional consideration of the solar beam trajectory and hence neglects shading due to canopy interception of direct radiation. A third model ($P09_{gap}$) is presented that explicitly treats shade and transmittance dynamics in and around idealized cylindrical forest gaps depending on solar angles and the spatial position relative to the center of a gap with a given radius and canopy height. This spatially distributed model is formulated in terms of canopy path length similar to the two models described previously, but the path length is modified to account for the presence of a canopy gap that can reduce the distance that a beam would travel through a continuous forest canopy. In this model, the direct beam canopy transmittance at spatial position (i, j) on the forest floor ($z = 0$) at time t when the sun is above the horizon (i.e., $\theta_t > 0$) is estimated as in Eq. (3) as:

$$\tau_{dir_{i,j,t}} = e^{-(\mu_t \ell_{c_{i,j,t}})}, \theta_t > 0 \tag{8}$$

Unlike Eq. (4) in which ℓ_t was the path length through a continuous and homogeneous forest, $\ell_{c_{i,j,t}}$ in Eq. (8) is the path length of a beam traveling only through the canopy and excludes the distance traveled through the forest gap. To solve for $\ell_{c_{i,j,t}}$, ray tracing is performed to determine potential intersection(s) between a ray

originating at the ground surface and traveling in the direction of the sun and a single canopy gap idealized as an upright circular cylinder of height H and radius r in 3-D Cartesian space. The model is fully described in Appendix A. Note that a constant $L' = 2.95$ was specified as the baseline forest effective plant area index as in $P09_{bulk}$.

2.2. Study area and validation dataset

A medium-size forest gap in the Marmot Creek Research Basin, Alberta, Canada (50°57′N, 115°09′W; 1860 m above sea level) was selected as a model validation site (Fig. 1). The gap was approximately 56 m in diameter and deviated from a circular shape as illustrated in Fig. 1. The dense surrounding forest had an average height of 13 m and was composed primarily of Engelmann spruce, subalpine fir, and a few lodgepole pines (Kirby and Ogilvy, 1969). Note that the gap radius was slightly more than twice the canopy height, or 2H. In general, the conifer forest canopy was vertically continuous from the top to nearly the snow surface such that the vertical depth of scattering elements h in Eq. (4) was specified to be equivalent to the average tree height H. The relatively level (slope <5%) site was located on an otherwise steeper mountainside rising to a ridgeline immediately to the west that resulted in terrain shading late in the day (Marsh et al., 2012). Above-canopy solar irradiance (unaffected by surrounding trees) was measured atop a 15 m meteorological tower located in the center of the gap (Fig. 1).

Solar radiation measurements used for model validation were collected on May 6, 2013 with an array of 20 Kipp & Zonen CM3 pyranometers (spectral sensitivity: 305–2800 nm). Fig. 1 shows the spatial arrangement of the 20 sensors positioned along an approximate north–south axis of the gap and extending 15 m into the forest on both sides. A greater density of sensors was deployed on the south side of the gap to capture shading by the forest edge, and in the forest to the north of the gap to measure enhanced transmittance beyond the gap extent due to reduced canopy path lengths. Note that four Kipp & Zonen CNR4 radiometers were located in the gap center between sensors 10 and 11 (Fig. 1) and nearest the north and south gap edges, but were not used in the analysis to maintain consistency of sensor type and height. Sensors were placed on rigid foam blocks on the snow surface and were carefully cleaned and levelled the previous evening and throughout the day. Data were measured at 10 s intervals and averaged and recorded every 5 min as in Lawler and Link (2011).

At each of the 20 pyranometer locations, upward-looking hemispherical photos were obtained using a tripod-mounted Nikon

Table 1
Sensor-specific model evaluation.

	Sensor	Norm. cumulative error			RMSE			Bias, W m^{-2}			R		
		Bulk	SVF	Gap	Bulk	SVF	Gap	Bulk	SVF	Gap	Bulk	SVF	Gap
South forest	1	−0.59	−0.59	−0.28	95.5	95.3	86.8	−25	−24.6	−12	0.39	0.39	0.5
	2	0	−0.01	0.75	29.4	29.5	35.3	0	−0.2	12.7	0.35	0.35	0.31
	3	−0.31	−0.18	0.28	34.7	33.7	34.1	−7.5	−4.4	6.7	0.43	0.44	0.47
	Mean	−0.3	−0.26	0.25	53.2	52.8	52.1	−10.8	−9.7	2.5	0.39	0.39	0.43
Shaded open	4	14.32	1	0.35	526.1	45.9	29.8	427.5	29.8	10.5	0.53	0.53	0.55
	5	8.48	0.49	−0.02	506.8	67.7	60.7	409.1	23.6	−0.8	0.43	0.43	0.43
	6	3.69	0.1	0.01	459	149.6	147.9	359.9	10.1	1.1	0.47	0.47	0.48
	7	1.04	−0.29	0.04	366.8	253.7	230	233.5	−65.4	9.3	0.58	0.58	0.62
	Mean	6.88	0.32	0.1	464.7	129.2	117.1	357.5	−0.47	5	0.5	0.5	0.52
Sunlit open	8	0.23	−0.47	0.01	230.1	320.2	222.3	84.6	−176.9	5.1	0.81	0.81	0.8
	9	−0.03	−0.55	−0.09	122.3	352.9	115.2	−15	−257.9	−41.1	0.95	0.95	0.96
	10	0.12	−0.45	0.1	111.6	323.2	98.1	−17.8	−233.4	−29.9	0.96	0.96	0.97
	11	−0.02	−0.45	−0.05	116.5	299.3	62.5	−9.5	−211.2	−24.2	0.97	0.97	0.99
	12	0.03	−0.54	−0.06	111.7	337.6	73.9	14.2	−240.5	−26.3	0.96	0.97	0.98
	13	0.12	−0.67	−0.03	160.8	403.3	81.4	50.4	−274.3	−11.5	0.93	0.94	0.98
	14	0.12	−0.76	−0.07	180.7	457.6	64.9	50.7	−308.4	−27.9	0.92	0.94	0.99
	Mean	0.08	−0.56	−0.03	147.7	356.3	102.6	49.7	−232.9	−14.5	0.93	0.93	0.95
North forest	15	1.11	−0.74	0.18	356.5	335.3	239.4	240	−161	40	0.67	0.79	0.71
	16	−0.3	−0.25	0.44	71.6	71.3	102.3	−12.6	−10.4	18.5	0.28	0.28	0.13
	17	−0.36	−0.29	−0.11	103.1	102.6	109.5	−16.9	−13.5	−5.2	0.22	0.22	0.11
	18	−0.05	0	−0.03	44.3	44.3	44.3	−1.6	−0.1	−0.9	0.44	0.44	0.44
	19	0.15	0.04	0.13	50.9	50.7	50.9	3.8	1	3.3	0.37	0.37	0.37
	20	0.03	−0.01	0.03	50.2	50.2	50.2	0.8	−0.2	0.8	0.48	0.48	0.48
	Mean	0.09	−0.21	0.11	112.8	109.1	99.4	−5.3	−4.6	3.3	0.41	0.43	0.37
	All sensors	1.39	−0.23	0.08	186.4	191.2	97	88.4	−95.9	−3.6	0.61	0.61	0.61

Coolpix 995 camera with a fisheye converter. Photos were taken at a height of 1 m above the sensor level. Images were processed with the CANEYE software (Baret and Weiss, 2004) to estimate the in situ sky view factor (v). The sensor-specific v values were used in all three (point-scale) models to estimate τ_{dif} in Eq. (2), and in the P09$_{SVF}$ model to scale the direct beam transmittance according to L' in Eq. (6). Differentially corrected UTM coordinates of the sensors and tower were obtained with a Leica Viva GS15 base station and rover. An airborne LiDAR-derived DEM and canopy density map (DeBeer and Pomeroy, 2010; Hopkinson et al., 2012), at 1 m grid spacing, are provided in Fig. 1 to illustrate the gap and canopy structure relative to the sensor and tower locations.

The projected circular outline of a conceptual canopy gap (56 m diameter) used in the P09$_{gap}$ model is also shown (Fig. 1). The circle was georeferenced to most closely align with the LiDAR-measured canopy edge and the model was run at the point-scale by converting pyranometer UTM positions to circle-centric Cartesian coordinates (see Appendix A).

2.3. Experimental design

The three models were evaluated for their relative skill at simulating the solar irradiance measured at the 20 sensor locations in and around the forest gap for this clear day. Three error metrics were evaluated: the normalized cumulative daily error (NCE), the root mean square error (RMSE), and the model bias. The three models were then applied in a spatially explicit manner (131 × 131 m, 1 m grid spacing, with the gap center offset in the southern 1/3 of the domain) to compare model estimates of cumulative daily irradiance in and around the conceptual cylindrical gap (Fig. 1). The models were forced with the same above-canopy shortwave observations as described previously.

For ease of discussion, sensors positioned in and around the forest gap are classified into four regions of similar irradiance: (i) south forest (3 sensors); an area of low irradiance caused by direct beam attenuation by continuous canopy and limited gap influence on diffuse radiation, (ii) shaded open (4 sensors); an area on the south side of the gap that received reduced irradiance as a result of shading from the forest on the southern edge of the gap, (iii) sunlit open (7

sensors); an area inside the gap with a large sky view that received full irradiance for much of the day, and (iv) north forest (6 sensors); an area of forest with reduced irradiance on the north side of the gap but some direct and diffuse contributions from the gap into the forest. Model results are compared within and among these general irradiance regimes; the suitability of the irradiance regime classification is further evaluated against measurements.

Finally, a clear-sky sensitivity test of the P09$_{gap}$ model was conducted. Above-canopy, clear-sky global, direct and diffuse solar radiation components were estimated as in Allen et al. (2006) with solar positions calculated as in Reda and Andreas (2004) using a solar constant of 1367 W m^{-2}. The above-canopy data were estimated for biweekly intervals between December 21 and June 22 at five-minute daylight time steps (SW$_{0\downarrow_t}$ > 0) for latitudes between 31°N and 71°N representing the general latitudinal extent of North American coniferous forests. For each latitude and date range, the model was run with canopy gap radii (fraction of the 13 m forest height, H) ranging from 2 m (0.15H), to 50 m (3.85H).

The sensitivity results of the effects of latitude, date, and gap size on sub-canopy solar irradiance in and around forest gaps were evaluated as follows. First, illustrative examples of model results from changing latitude and day of year for a single gap size (1H) are provided. Three model metrics are presented: (i) the cumulative daily solar irradiance, (ii) the fraction of global cumulative daily irradiance composed of the direct solar beam, and (iii) the cumulative daily solar irradiance normalized by that simulated in a continuous forest i.e., the fraction of irradiance contributed by the gap itself, referred to as the Normalized Gap-Contributed Irradiance (NGCI).

The location and magnitude of the daily cumulative radiative maxima were evaluated. This metric informs where, relative to the gap center, the solar irradiance is greatest, how that location changes with solar angle and gap size, and how the magnitude compares to the above-canopy value. Finally, metrics describing the cumulative daily irradiance (median, quartiles, and coefficient of variation CV) were used to evaluate the sensitivity of solar irradiance dynamics to latitude, gap size, and day of year separately for the area within the projected gap extent and in the forest beyond the gap. Because irradiance is a continuous two-dimensional field and very low magnitude irradiance transmitted through a gap can
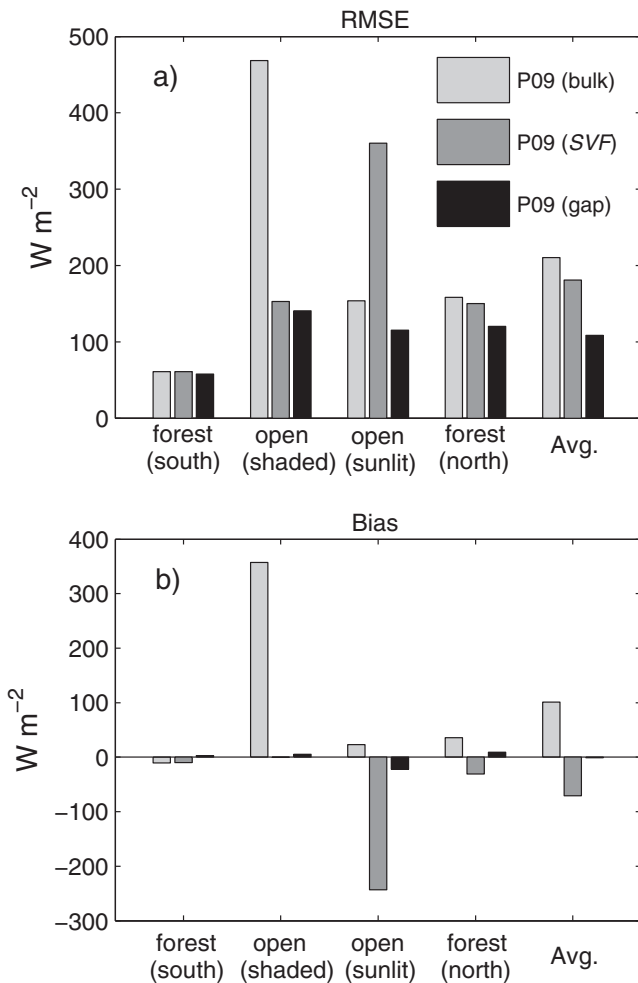
Fig. 4. (a) RMSE and (b) bias values of the three models computed against five-min measurements for May 6, 2013. Errors bars represent the mean model error binned according to the relative gap location: forest south ($n = 3$); open shaded ($n = 4$); open sunlit ($n = 7$); forest north ($n = 6$); and the average error for all sensor locations ($n = 20$).

extend long distances into the forest, a threshold of 5% above the continuous forest values was specified; values below 5% were not evaluated. This value was chosen to include as much of the area of gap influence within the model domain as possible (i.e., the area delineated by a lower threshold value may have extended beyond the model domain when solar elevation angles were low) and to capture as much of the variability as possible. Seasonal trends in these metrics were explored for their sensitivity to gap size and latitude.

3. Results

3.1. Measurements and models

Time-series comparisons of model results and measurements from sensor locations along south- and north-side gap transects illustrate the high spatiotemporal variability of solar radiation and the differences among the performances and simulated dynamics of the $P09_{bulk}$, $P09_{SVF}$ and $P09_{gap}$ models (Fig. 2). The temporal variability in measured solar irradiance increased from the gap center (Fig. 2a) toward the south (shaded) edge (Fig. 2c and e) and the duration of unimpeded irradiance decreased from the gap center (Fig. 2b) toward the north (sunlit) edge (Fig. 2d and f). Within the gap, the $P09_{SVF}$ model that scaled direct beam

transmittance only according to the proximal sky view greatly underestimated the irradiance compared to measured values, however $P09_{SVF}$ estimates were closest to measured irradiance values nearest the shaded gap edge (Fig. 2e and g). Comparatively, the $P09_{bulk}$ model simulated the magnitude of uninterrupted midday irradiance quite well at sun-exposed (hereafter, sunlit) sensor locations within the gap (Fig. 2a–d and f) including the sunlit canopy edge (Fig. 2h). Despite the midday accuracy at these locations, the $P09_{bulk}$ model overestimated the morning and afternoon irradiance values measured within the gap, particularly on the sunlit side (Fig. 2d, f, and h) and vastly overestimated midday irradiance on the shaded side throughout the day (Fig. 2e and g). The $P09_{gap}$ ray trace model simulated both the magnitude of measured uninterrupted irradiance and the reduced morning and afternoon irradiance values quite well. Although $P09_{gap}$ coarsely approximated the intermittent nature of measured irradiance values both on the shaded side of the gap (Fig. 2e) and the sunlit edge (Fig. 2h) with a bell-like curve of reduced magnitude, it exhibited the lowest spatially integrated error. For example, the spatially averaged RMSE values from the $P09_{bulk}$, $P09_{SVF}$ and $P09_{gap}$ models evaluated at four sensor locations within the shaded region of the gap were 464.7 W m^{-2}, 129.2 W m^{-2}, and 117.1 W m^{-2}, respectively (Table 1). On average at seven sensor locations within the sunlit gap region, the $P09_{bulk}$, $P09_{SVF}$ and $P09_{gap}$ models produced RMSE values of 147.7 W m^{-2}, 356.3 W m^{-2}, and 102.6 W m^{-2}, respectively (Table 1). Averaged at all sensor locations within the gap, the $P09_{bulk}$, $P09_{SVF}$ and $P09_{gap}$ models produced RMSE values of 306.2 W m^{-2}, 242.8 W m^{-2}, and 109.9 W m^{-2}, respectively, and bias values of 203.6 W m^{-2}, -116.7 W m^{-2}, and -4.8 W m^{-2}, respectively.

In the forest, measured irradiance values were low with short-duration spikes i.e., sunflecks, more prevalent north of the gap (Fig. 2j) than in the forest to the south (Fig. 2i). Here, $P09_{gap}$ simulated a slight increase in irradiance between 13:00 and 15:30 that was not simulated by the other two models (Fig. 2j). The difference was due to the $P09_{gap}$ model's ability to simulate a reduction in direct beam canopy path length in the early afternoon caused by the close proximity of the sensor location to the conceptual gap (see example in Fig. A1). Only in the forest to the south of the gap where direct beam transmittance was least likely to be impacted by the forest gap did the three models produce similar irradiance estimates (Fig. 2i).

When evaluated against sensor measurements made in the forest to the south of the gap, all three models generally performed well and no one model stood out as optimal (Table 1 and Fig. 3). Inside the gap, however, distinct differences between the three models were evident (Figs. 3 and 4; Table 1). Of all models, $P09_{bulk}$ had the greatest overall error; it greatly overestimated irradiance on the shaded south side of the gap (mean NCE, RMSE, and bias of 6.88, 465 W m^{-2}, and 357 W m^{-2}, respectively) as well as near the sunlit forest edge on the north side of the gap (Table 1; Figs. 3 and 4) because it ignored any effects of forest cover except that directly overhead. Despite high error values near the gap edge, $P09_{bulk}$ exhibited low error compared to sensor observations in the sunlit central part of the gap where its open sky assumptions for the gap were most closely met (mean NCE, RMSE, and bias of 0.08, 148 W m^{-2}, and 50 W m^{-2}; Table 1 and Figs. 3 and 4). The $P09_{SVF}$ model was most accurate nearest the shaded, southern gap edge (mean NCE, RMSE and bias of 0.32, 129 W m^{-2}, and 0.5 W m^{-2}), but the errors trended increasingly negative toward the northern, sunlit side (mean NCE, RMSE, and bias of -0.56, 356 W m^{-2}, and -233 W m^{-2}) and into the forest to the north (Fig. 3). Whilst $P09_{SVF}$ reduced transmittance according to proximal sky view it did not consider enhanced transmittance in the direction of the sun – the model thus performed best on the shaded side of the gap where solar transmittance was more diffuse-dominated (Fig. 2e and f). The
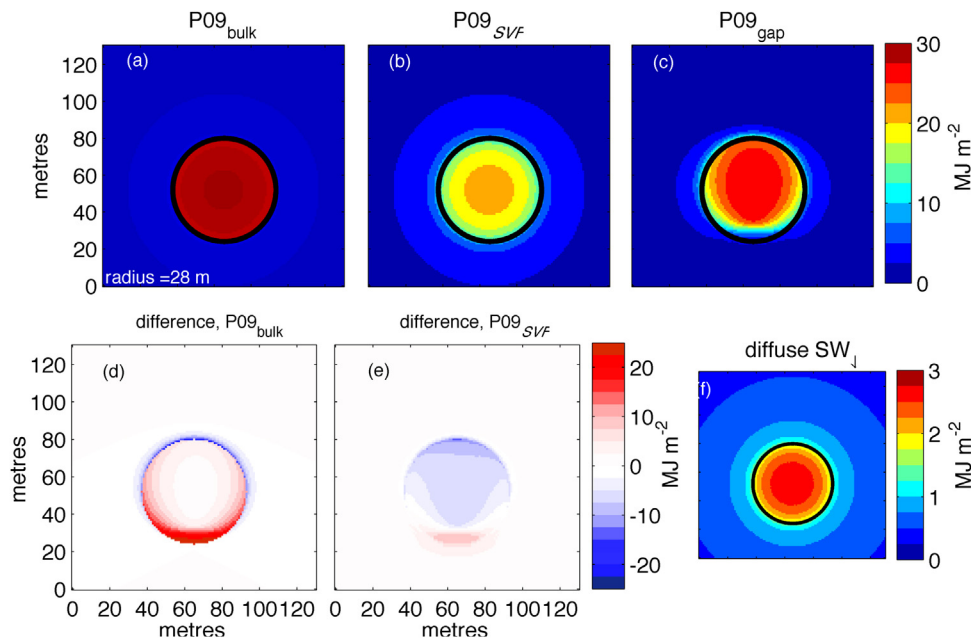
Fig. 5. (a–c) Spatially distributed cumulative global shortwave irradiance on May 6, 2013 modeled in and around a 28 m radius circular gap using the Pomeroy et al. (2009) (i.e., 'P09') model with (a) a bulk canopy treatment $P09_{(bulk)}$ (constant LAI' in forest; full transmittance in gap) and (b) variable gap transmittance $P09_{(SVF)}$ (constant LAI' in forest; gap transmittance according to a distributed v estimate), and (c) the conceptual cylindrical gap path length model $P09_{(gap)}$. (d–e) The differences in the $P09_{(bulk)}$ and $P09_{(SVF)}$ model results compared to the $P09_{(gap)}$ model (i.e., 'P09xxx–$P09_{(gap)}$'). (f) The diffuse irradiance estimated from v for all three models.

$P09_{gap}$ model exhibited low errors at all sensor locations within the gap (mean NCE, RMSE and bias of −0.04, 110 W m^{-2}, and −5 W m^{-2}) and, unlike the other models, there was no trend in error from the south (S) to the north (N) side (Figs. 3 and 4). When averaged over the 20 sensor locations, the $P09_{gap}$ model outperformed the $P09_{SVF}$ and $P09_{bulk}$ models in terms of the NCE (0.07, −0.23, and 1.38, respectively), RMSE (108 W undefined m^{-2}, 181 W m^{-2}, and 210 W m^{-2}, respectively) and bias (−1.3 W m^{-2}, −71.1 W m^{-2}, and 101.0 W m^{-2}, respectively) error metrics (Figs. 3 and 4).

When applied to the complete spatial domain, the differences in cumulative solar irradiance simulated by the three models were large (Fig. 5). All three models treated diffuse irradiance similarly (Fig. 5f) such that differences in cumulative irradiance (Fig. 5a–c) are caused by differences in calculation of direct beam transmittance. The bulk approach simulated high solar irradiance (28 MJ m^{-2}) throughout the gap whereas the proximal sky view approach simulated a maximum irradiance at the gap center of 19 MJ m^{-2}, symmetrically dropping to 13 MJ m^{-2} at the gap edge (Fig. 5b). The $P09_{gap}$ model estimated asymmetry in cumulative solar irradiance patterns along the N–S axis in and around the gap with a maximum value (28 MJ m^{-2}) at the center and a minimum value (<5 MJ m^{-2}) against the southern gap edge (Fig. 5c). Notably, the $P09_{gap}$ model simulated higher solar irradiance (>10 MJ m^{-2}) than the other models in the forest to the N, east (E), and west (W) of the gap – this zone of enhanced irradiance within the forest was limited to within 10 m of the gap edge. Compared to the $P09_{gap}$ cumulative irradiance simulated for this single day of measurement (May 6, 2013), the bulk approach greatly overestimated (>20 MJ m^{-2} difference) and underestimated (<−18 MJ m^{-2} difference) irradiance along the S side of the gap and within the forest on the N side, respectively (Fig. 5d). The proximal sky view model slightly overestimated irradiance on the S side of the gap and largely underestimated irradiance in the center and on the N side of the gap as well as into the forest, particularly on the N side (Fig. 5e). Given these persistent differences in model performance and insight into gap solar radiation dynamics, the $P09_{gap}$ with its minimal errors was employed for further sensitivity analysis.

3.2. Forest gap model sensitivity to latitude, day of year, and gap size

Simulations with the $P09_{gap}$ model showed that changing latitude and day of year had pronounced impacts on the magnitude and spatial patterns of the cumulative daily solar irradiance in and around a 1H radius gap (Fig. 6; left panels). The magnitude of cumulative solar irradiance increased seasonally at all latitudes. The spatial patterns were symmetric about the N–S gap axis (as in Fig. 5c) but highly asymmetric about the E–W axis with a region of enhanced irradiance to the north of gap center and elongated in the E–W direction (Fig. 6; left panels). Comparatively low irradiance was simulated S of the gap center. In general, the N–S asymmetry became less pronounced with time since the winter solstice and this trend was consistent across all but the highest latitudes (Fig. 6; left panels). The simulated N–S asymmetry was caused by enhanced direct beam transmittance to the N of gap center, where the direct beam fraction of cumulative irradiance often exceeded 90%, compared to the S side of the gap where it represented only 50–70% (Fig. 6; right panels). The direct beam was the dominant solar flux to distances as far as 2H beyond the gap edge into the surrounding forest (Fig. 6; right panels). The Normalized Gap-Contributed Irradiance NGCI metric in Fig. 7 illustrates the spatial extent of gap influence on cumulative solar irradiance; the greatest influence (NGCI > 3) was always within 2H of the gap center (1H of the gap edge) whereas low-level influence (NGCI < 3) extended distances >2H into the forest particularly to the N of the gap at higher latitudes and early in the year.

The spatial location of the maximum cumulative irradiance relative to the gap center varied with gap size, time of year, and latitude (Fig. 8). In small gaps ≤1H radii in midwinter, the irradiance maxima (<10% of above-canopy radiation) occurred at the N edge of the gap except at latitudes ≥51°N, where lower winter solar angles created predominantly diffuse radiation that caused the maxima to occur closer to the gap centers (Fig. 8a). Later in the season as solar angles increased, the maxima irradiance values in small gaps at these higher latitudes (≥51°N) trended toward the N edge of
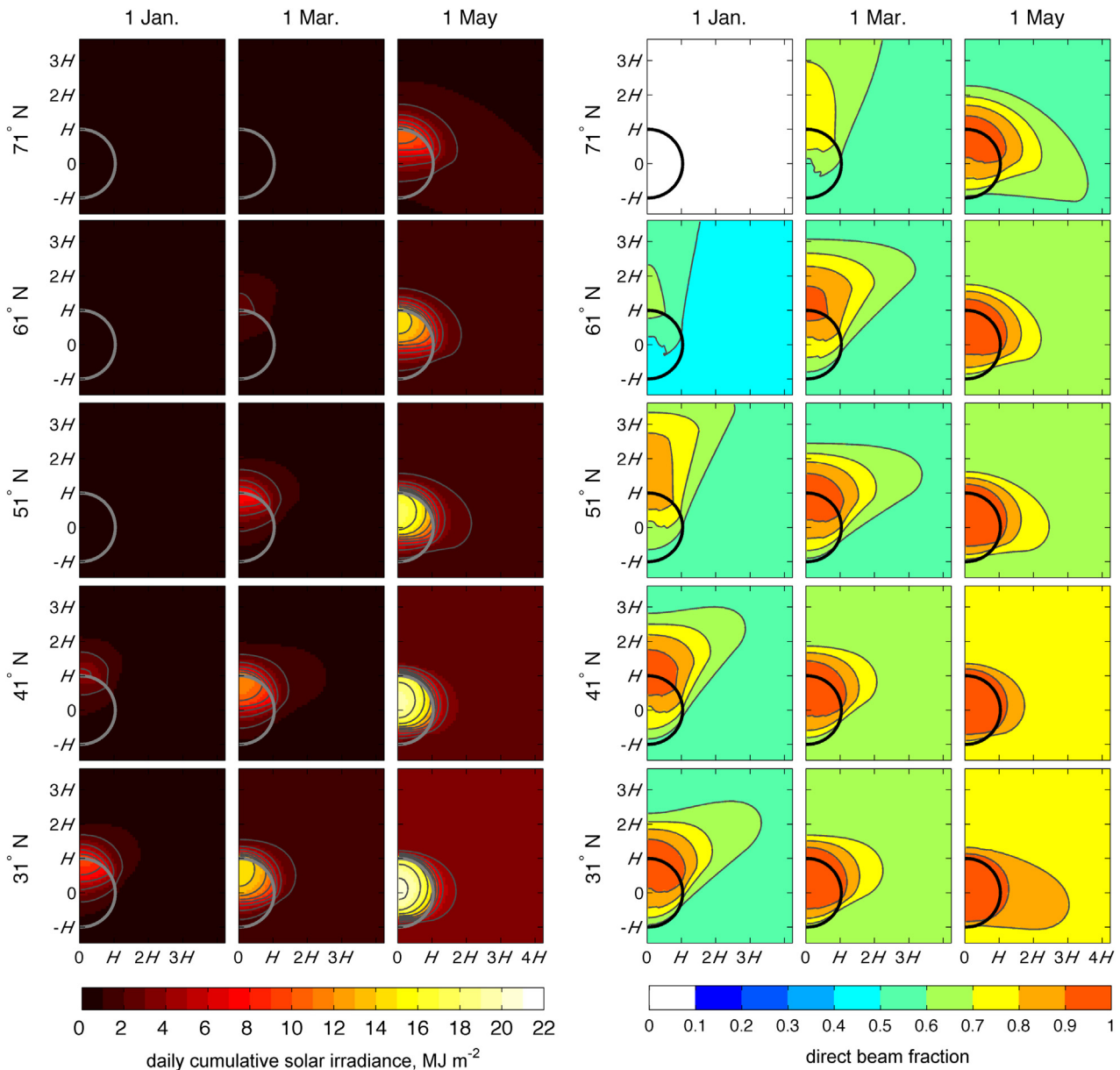
Fig. 6. (left) Simulated daily cumulative solar irradiance in and around a gap with a radius length equal to the forest height (1*H*) for five latitudes (panel rows) for the first days of January, March and May (panel columns; (right) the direct beam fraction of cumulative daily global solar irradiance for a 1*H* gap and for the same range of latitudes and days. Circular outlines of the projected gap are shown. Note that the gaps are offset in the southern 1/3 of the domain to highlight the enhanced irradiance patterns to the N of the gap, and only the eastern half of the domains are shown as results are symmetrical about the N–S gap axis (see Canham, 1988).

the gap before again progressing closer to the gap center (Fig. 8b and c). In general, the magnitudes of gap irradiance maxima, relative to above-canopy values, exhibited similar trends throughout the year for all gap sizes and latitudes (Fig. 8). Note that the simulated cumulative daily irradiance maxima never occurred beyond the projected gap extent.

Within the extent of circular gaps (i.e., excluding the forest), the median cumulative solar irradiance was greater at lower latitudes, closer to the summer solstice, and in larger gaps (Fig. 9; left panels). Increasing gap size had a nonlinear positive effect on cumulative irradiance; increasing gap size at 51°N on May 1 from 0.5*H* to 1*H* radii resulted in a nearly three-fold increase in the (spatial) median cumulative irradiance of 9 MJ m^{-2} while further increasing from 1*H* to 1.5*H* caused only a 25% increase of 3.6 MJ m^{-2}. Within the gaps, the distribution of the median daily cumulative solar irradiance was biased toward the third quartile for high solar elevations and larger gaps and slightly biased toward the first quartile for small gaps

under conditions of low solar elevations (Fig. 9; left panels). The coefficient of variation CV of cumulative daily solar irradiance was greatest at lower latitudes, in smaller gaps, and early in the winter; a trend that reversed with increasing gap size and in the spring when the CV became positively correlated with latitude (Fig. 9; right panels). The gap size at which the CV on a given date was maximized was latitude and date dependent. For example, at 51°N latitude the maximum CV value (0.84) occurred for a 2.15*H* gap on January 1, the maximum CV was 0.71 for a 1*H* gap on March 1, and 0.48 for a 0.5*H* gap on 1 May (Fig. 9; right panels).

4. Discussion

Measurements of global solar radiation at 20 sensor locations along a N–S transect of a forest gap on May 6 at 51°N latitude indicated sharply different irradiance regimes over short distances and time periods. Measurements made nearest the gap center were,
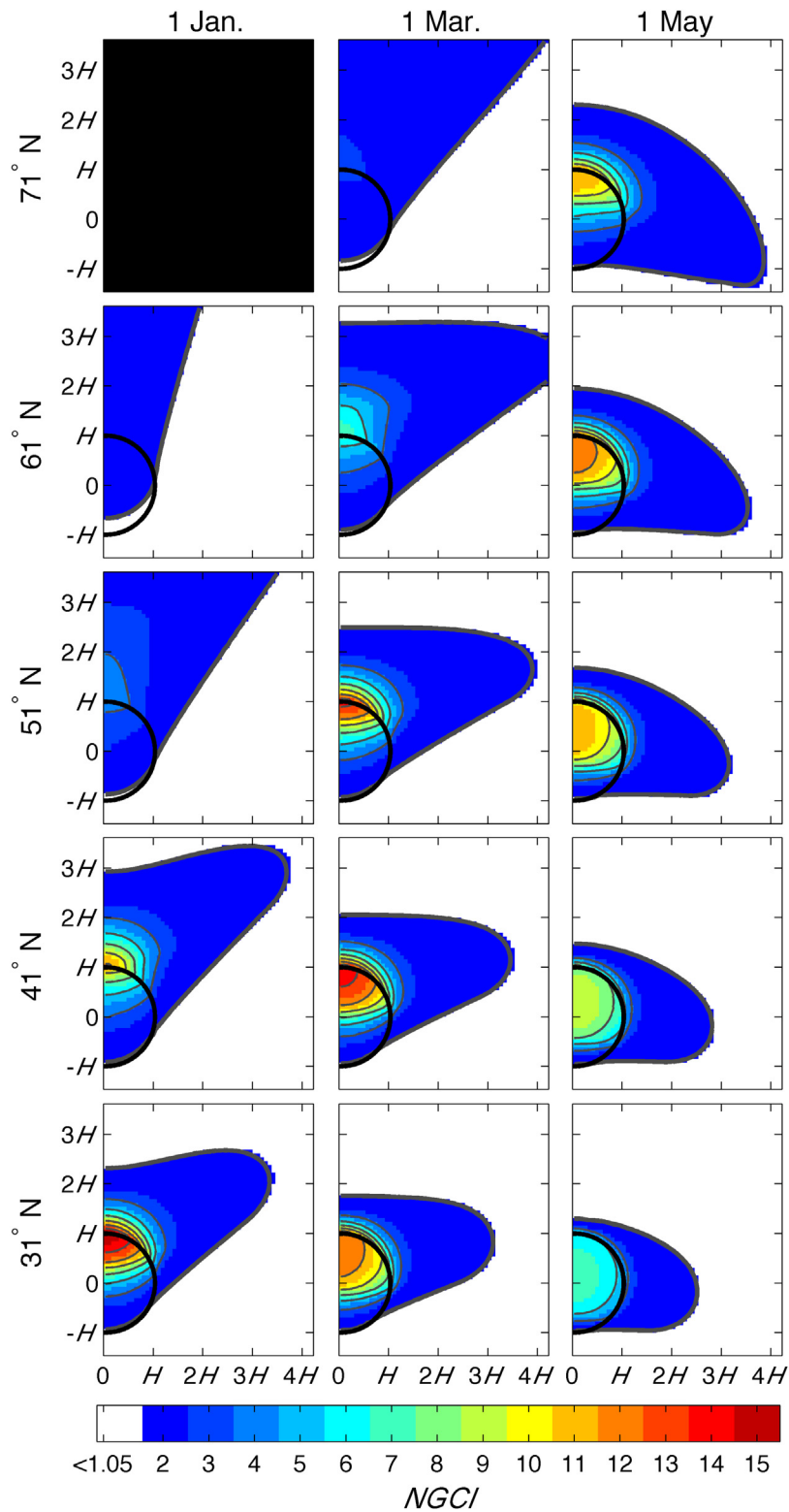
Fig. 7. The fraction of solar irradiance relative to a continuous forest (i.e., Normalized Gap Contributed Irradiance, NGCI) in and around a 1H gap for a range of latitude (panel rows) and dates (panel columns). A threshold of 5% above the cumulative irradiance estimated in a continuous forest i.e., NGCI ≥ 1.05 was used to limit the (otherwise semi-infinite) spatial extent of the NGCI metric.

at mid-day, the closest in form to the bell-shape of the measured cloud-free above-canopy irradiance (Fig. 2a and b). The steeper limbs and narrower shape of the irradiance at gap-center were caused by direct beam extinction by the forest edges in the morning and evening. This irradiance regime also extended into the N

side of the gap (Fig. 2). In contrast, the S side of the gap was subject to intermittent shading by individual trees of different heights that comprised the forest edge, which produced alternating irradiation in the form of full sun and shade. Toward the S gap edge, the transmitted radiation environment was increasingly diffuse and
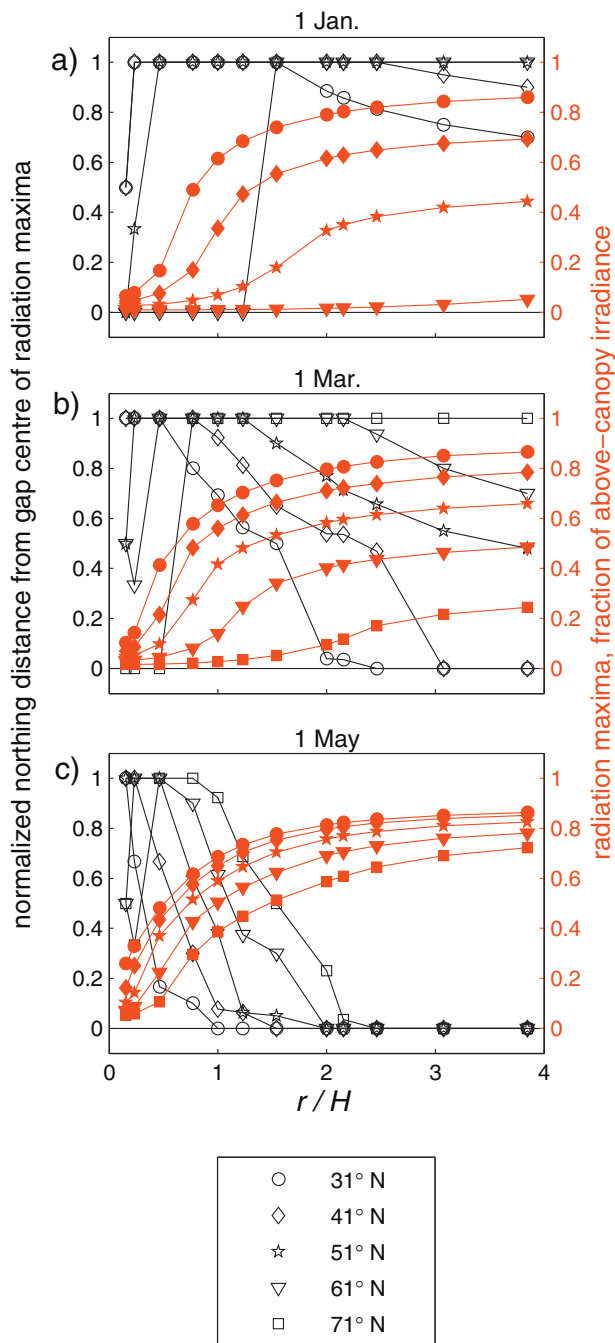
Fig. 8. Location (normalized northing distance from gap center where 0 and 1 correspond to the gap center and northern gap edge, respectively; hollow black markers) and magnitude (fraction of above-canopy irradiance; filled red markers) of the cumulative shortwave radiation maxima estimated by the gap model for the 1st day of the months of January (top), March (middle), and May (bottom) as a function of changing the circular gap radius length r (x-axis; provided as a fraction of canopy height H) for five different latitudes (symbols). (For interpretation of the references to color in this figure legend, the reader is referred to the web version of this article.)

received fewer and shorter duration periods of direct beam radiation (Fig. 2). Direct beam radiation also penetrated from the gap up to 10 m N into the forest (Fig. 2i) and periods of direct beam radiation from the gap were more frequent and prolonged relative to those due to sunflecks on the forested S side (Fig. 2j). This finding supports the concept of gap influences extending beyond the projected gap area as initially suggested by Runkle (1982). The measurements and simulations illustrate the dynamic and complex nature of shortwave energy gradients in and around a moderate-size canopy clearing (2H radius).

Compared to measurements, models that did not explicitly resolve shading and enhanced canopy transmittance were incapable of reliably simulating the spatial variability or daily mean properties of irradiance in and around the forest gap. The binary, tiled $P09_{bulk}$ model that ignored shading performed best in locations where its underlying uniform assumptions were most realistic: in the continuous forest to the S that did not receive direct radiation from the gap, and in the center and N sectors of the gap that had minimal shading from the surrounding forest. Adjustments to the direct beam transmittance based on proximal sky view ($P09_{SVF}$) performed better where $P09_{bulk}$ failed, but exhibited large negative biases over other parts of the gap and overestimated irradiance near the shaded S edge (Figs. 3 and 4). The results illustrate the importance of considering process-based shading and transmittance dynamics in the estimation of solar irradiance in and around a forest gap.

It is shown that when the model representation of the direct beam canopy path length is modified to account for canopy gaps, accurate simulations of irradiance in and around a forest gap are possible. The main limitation of the ray trace model is the assumption that the gap is surrounded by a homogeneous canopy structure. Errors from forest conditions not meeting this assumption were most prevalent around the irregular gap edges (Figs. 3 and 4). These challenges for canopy solar transmittance models are well documented (e.g. Canham et al., 1990; Lawler and Link, 2011; Musselman et al., 2012; Nijssen and Lettenmaier, 1999) and could be overcome with a spatially distributed representation of canopy structural variability and thus improved representation of 3-D canopy path lengths such as can be obtained with LiDAR (e.g., Musselman et al., 2013; Peng et al., 2014). Finally, the instrumented gap deviated in shape from a conceptual cylinder and an access road to the southeast (Fig. 1) that resulted in increased morning transmittance at sensors 7–10 and a corresponding underestimation of irradiance by the $P09_{gap}$ model (Fig. 2a and c).

Patterns of daily areal solar irradiance simulated by the spatially explicit $P09_{gap}$ model varied according to the day of year, latitude and gap size (Figs. 6 and 7). Lower solar angles promoted a marked N–S asymmetry in irradiance, with more gap-contributed irradiance on the N side of the gap and in the adjacent forest; this asymmetry was more common at higher latitudes and declined as solar elevation increased into the spring months. Canham et al. (1990) reported a similar asymmetry and found that maximum growing-season gap PAR occurred nearest the gap center at low latitudes (10°N) and migrated toward and sometimes beyond the northern gap edge as latitude increased and/or gap size decreased. The extended sensitivity analysis to earlier in the season, more northerly latitudes, and to larger gaps expands upon previous results to show that the spatial location of maximum irradiance occurs near gap center when the irradiance regime is diffuse-dominated (i.e., earlier in the year, at higher latitudes, and in smaller gaps) (Fig. 8). An abrupt shift in the spatial location of the irradiance maximum to the northern gap edge occurs as sufficiently high solar elevation angles and/or large gap sizes permit the direct beam to pass unimpeded into the gap; this shift is followed by a gradual progression of the irradiance maximum back to the gap center (as reported by Canham et al., 1990) as solar elevation angles/gap sizes further increase (Fig. 8). Interestingly, the simulated position of maximum irradiance did not migrate into the forest, even for small gaps at high latitudes (Fig. 8). In contrast, Canham (1988) reported maxima values as far as 5 m (1 gap radius) N of the northern gap edge for a 0.2H gap at 44°N during the summer growing season when solar elevations were relatively high. As the Canham (1988) beam transmittance algorithm was not published, the cause of the discrepancy remains unknown. In general, there is
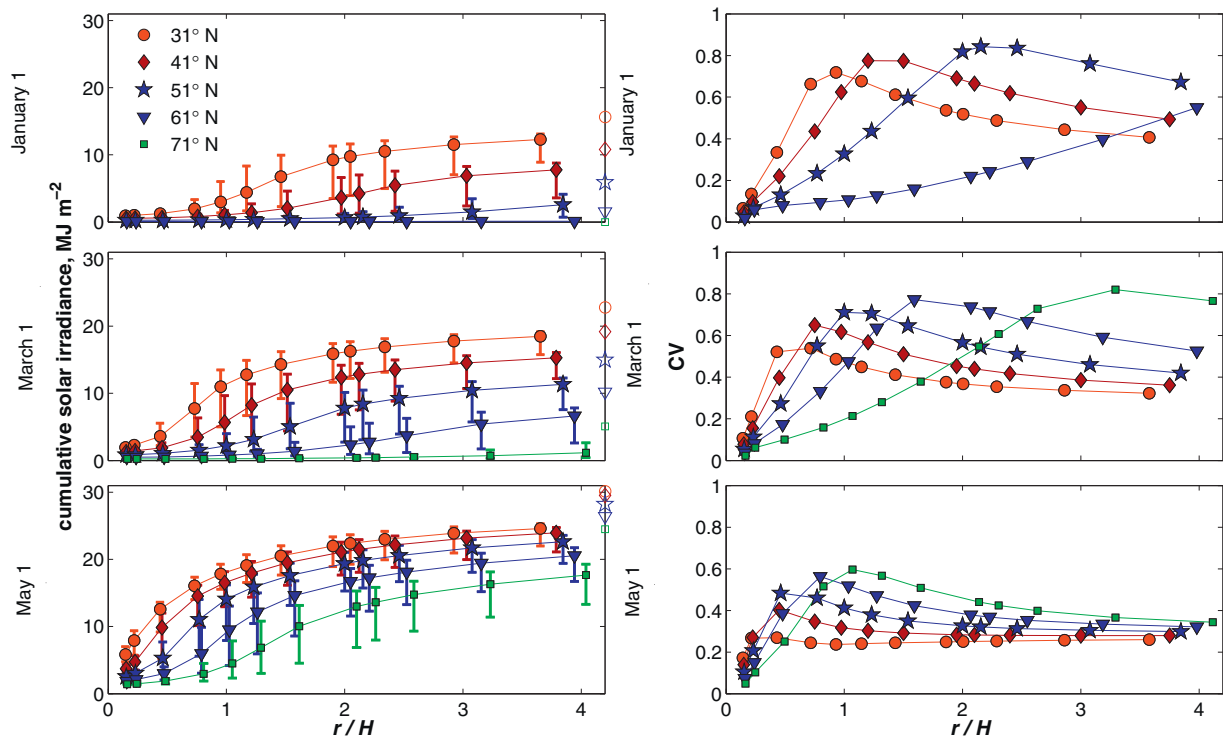
Fig. 9. (left) Cumulative solar irradiance (*y*-axes) within the circular gap extent reported as the median (markers) and quartiles (bars) for a range of latitude (marker style, color), gap size (*x*-axes), and date (panel rows). The empty markers on the right *y*-axis indicate the above-canopy cumulative irradiance for the respective latitudes (i.e., that expected in a gap of infinite size). (right) The coefficient of variation CV of the cumulative solar irradiance values within the circular gap extent for the same sensitivity analysis. Markers are offset along the *x*-axes for visual clarity.

strong agreement between the two studies in that nearly half of the gap-contributed irradiance, largely dominated by the direct beam, occurred in the northern sector of gaps (Fig. 7) and often extended well into the forest, particularly when solar elevations were low.

Forest structure characteristics used in the sensitivity analysis were derived from measurements made at the field site in the southern Canadian Rockies at 51°N. Because other latitudes and elevations will exhibit different primary forest characteristics such as LAI' and hence canopy extinction efficiency, and seasonal cloudiness will differ from the clear-sky assumption made here, the sensitivity results are idealized; gap influences on local solar irradiance will depend upon local forest characteristics and cloud cover and will vary in more complex ways than evaluated here.

The dynamics of the (spatial) distribution of shade and irradiance patterns simulated within a forest gap were indeed found to be sensitive to gap size, but the sensitivity was unique to latitude and day of year. In general, increasing gap size caused the median and quartiles of the irradiance distribution to first slowly increase for small (<1*H* radius) gaps, followed by a greater increase at mid-sized gaps, after which the curve begins to plateau for larger gaps (Fig. 9; left panels). The 'break' in the rate of increase of the irradiance median with gap size describes a condition where gap geometry and/or solar angles permit direct solar irradiance to predominantly fill a forest gap. It is useful to describe this 'break' in terms of the (spatial) variability of solar irradiance relative to the mean (i.e., the CV). Pomeroy et al. (2001) first described the CV of melt energy under a boreal forest canopy and found that it was normally distributed and suggested that it would be strongly influenced by forest shading and important to consider in deriving snow covered area depletion curves. The CV of shortwave irradiance within a gap was low for small gaps and low solar elevation angles when gap irradiance was diffuse dominated and varied largely according to sky view. At greater solar elevation angles and/or gap sizes, the CV increased as more direct beam radiation was allowed to pass over

the treetops into the gap, in sharp contrast to the shaded southern half of a gap. The CV increase with gap size was followed by a decrease, causing a global maximum CV value, as direct beam irradiance became the dominant flux and the area shaded by the forest edge was proportionately reduced (Fig. 9; right panels). This variation in a critical energy balance term for snow ablation provides an important first step in determining the spatial variation of melt energy in discontinuous canopies to inform future snow covered area depletion schemes that include variable melt energy.

5. Conclusions

A spatial comparison of three canopy transmittance models highlighted the importance of simulating shade effects of the forest edge in the direction of the sun as well as localized enhanced transmittance of solar radiation through the gap into the surrounding forest. A sensitivity experiment with a new canopy gap – ray trace model in which gap size, latitude, and day of year were varied showed remarkable spatial variability in cumulative daily solar irradiance. Lower solar angles promoted a north-south asymmetry in irradiance with greater irradiance on the northern half of the gap and in the adjacent forest; this asymmetry was more pronounced at high latitudes and declined as solar elevation angles increased after winter. The spatial distribution patterns of cumulative daily solar irradiance were evaluated; increasing gap size caused the (spatial) coefficient of variation CV to increase before reaching a latitude- and date-specific maximum, after which it decreased. This variability in shortwave irradiance – a critical snow energy balance term – can help to determine the spatial variation of melt energy to inform future snow covered area depletion schemes that include variable melt energy. The gap size at which the CV was maximized was used to describe a condition where gap geometry and/or solar angles permit direct beam solar irradiance to become the

predominant solar flux on the floor of a forest gap; smaller (larger) gaps were more diffuse (direct beam) dominated with reduced spatial variability relative to the mean. Future research should be able to extend this study to address gap influences over a range of forest stand characteristics, climate, and slopes at various latitudes. Future work should also incorporate the full suite of forest snow mass and energy exchange processes to determine optimal gap size for snow retention and methods to incorporate gap effects in basin and landscape scale snow models.

Appendix A.

The ray trace model used to compute the path length $\ell_{c_{i,j,t}}$ of a beam traveling through a canopy excluding the distance traveled through a forest gap idealized as a circular cylinder is presented here. To solve for $\ell_{c_{i,j,t}}$, the potential intersections, or quadratic roots λ, between a ray originating at the ground surface and traveling in the direction of the sun and a canopy gap idealized as a cylinder in 3-D Cartesian space (Fig. A1) are analytically evaluated. A ray is defined by its origin $M = (x_0, y_0, z_0)$ and a difference vector $D = (x_D, y_D, z_D)$ represented by the equation:

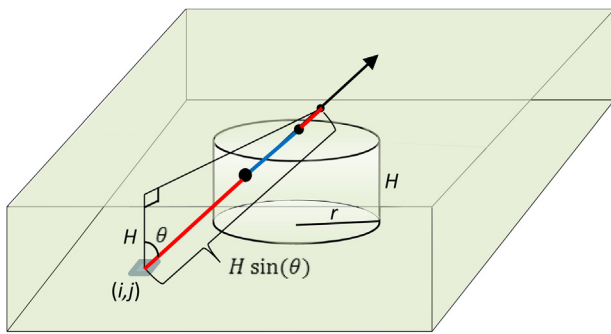$$P(\lambda) = M + \lambda D, \lambda \geq 0 \tag{A1}$$

Fig. A1. Illustration of a canopy gap conceptualized as a circular cylinder of radius r surrounded by a continuous and homogeneous canopy cover of height H. An illustrative example is provided of a ray initialized at grid element (i, j) on the forest floor and traveling at an elevation angle of θ a distance $H\sin(\theta)$ before emerging out the top of the canopy layer. Intersection points (filled circles) between the ray and the cylinder or top of the canopy layer are indicated. The intersection points are used to compute the path length of the ray through the canopy ($l_{c_{i,j,t}}$; red line elements) excluding the distance traveled through the canopy gap (blue line element). The example is representative of $l^{case5}_{c_{i,j,t}}$ from Eq. (A12). (For interpretation of the references to color in this figure legend, the reader is referred to the web version of this article.)

Since the ray is considered to originate at the ground ($z_0 = 0$), it can be represented by the equations:

$$\left.\begin{array}{l} x(\lambda) = x_0 + \lambda x_D \\ y(\lambda) = y_0 + \lambda y_D \\ z(\lambda) = 0 + \lambda z_D \end{array}\right\} \lambda \geq 0 \tag{A2}$$

The equation for a circular cylinder oriented along the z-axis with height H and radius r is:

$$x^2 + y^2 = r^2, \text{with} 0 < z \leq H \tag{A3}$$

Intersection points (if any) are solved for by plugging the ray equations (Eq. (A2)) into the cylinder equation (Eq. (A3)):

$$(x_0 + \lambda x_D)^2 + (y_0 + \lambda y_D)^2 = r^2 = \lambda^2(y_D^2 + x_D^2)$$
$$+\lambda(2x_0x_D + 2y_0y_D) + x_0^2 + y_0^2 \tag{A4}$$

and solving for λ (as many as two solutions). Positive λ values represent intersection points with an infinite cylinder (the finite case in terms of vertical boundaries is considered below). The quadratic equation can be solved as:

$$a = (y_D^2 + x_D^2) \tag{A5}$$

$$b = 2(x_0x_D + y_0y_D) \tag{A6}$$

$$c = x_0^2 + y_0^2 - r^2 \tag{A7}$$

A positive discriminant $b^2 - 4ac$ indicates the existence of at least one intersection, in which case the roots λ are calculated as:

$$\lambda = \frac{-b \pm \sqrt{b^2 - 4ac}}{2a} \tag{A8}$$

If a solution exists, the λ values are ranked from smallest (first intersection) to largest (last intersection), and the intersection point(s) I are computed as:

$$(I_x, I_y, I_z) = M + \lambda D \tag{A9}$$

Five possible intersection scenarios of a ray with a cylinder (gap) are considered:

Case 1) The ray originates outside of a gap ($x_0^2 + y_0^2 > r^2$) and does not intersect the gap edge. In this case, the beam travels entirely through the canopy and $\ell^{case1}_{c_{i,j,t}} = \ell_t$ (see Eq. (4)).

Case 2) The ray originates inside of a gap and does not intersect the gap edge (no intersection points satisfy $0 < I_z < H$). In this case, the beam travels entirely through the gap and $\ell^{case2}_{c_{i,j,t}} = 0$ making $\tau_{\text{dir}_{i,j,t}}$ in Eq. (8) reduce to 1 (the beam is fully transmitted).

Case 3) The ray originates outside of a gap ($x_0^2 + y_0^2 > r^2$), travels through the canopy until it intersects only one gap edge and exits out the top of the gap. The special case of a ray tangential to a canopy gap can cause errors in this assumption. If the discriminant is zero the ray is tangential and $\ell_{c_{i,j,t}} = \ell_t$. Otherwise, the path length traveled through the canopy is the distance from the ray origin to the single cylinder intersection and the canopy path length is:

$$\ell^{case3}_{c_{i,j,t}} = \sqrt{(x_0 - I_{x(1)})^2 + (y_0 - I_{y(1)})^2 + (z_0 - I_{z(1)})^2} \tag{A10}$$

Case 4) The ray originates inside of a gap ($x_0^2 + y_0^2 > r^2$). It travels through the gap until it enters the canopy by intersecting a single gap edge and exits out the top of the canopy. The path length traveled through the canopy is then the difference between ℓ_t and the distance from the ray origin to the single intersection:

$$\ell^{case4}_{c_{i,j,t}} = \ell_t - \ell^{case3}_{c_{i,j,t}} \tag{A11}$$

Case 5) The ray originates outside of a gap $(x_0{}^2 + y_0{}^2 > r^2)$ and has two intersection points with the gap (see Fig. A1). It travels through the canopy, enters and then exits two gap edges, and travels through more canopy until it exits out the top of the canopy. In this case, the path length traveled through the canopy is the difference between ℓ_t and the distance between the two intersections (i.e., the gap path length). The canopy path length is then:

$$\ell_{c_{i,j,t}}^{\text{case5}} = \ell_t - \sqrt{(I_{x(1)} - I_{x(2)})^2 + (I_{y(1)} - I_{y(2)})^2 + (I_{z(1)} - I_{z(2)})^2} \quad \text{(A12)}$$

To avoid a rare case that produces erroneous values, points located exactly on the radius of the cylinder $(x_0{}^2 + y_0{}^2 = r^2)$ are nudged toward the gap center by 0.1 m before the ray trace calculations are made.

References

Agee, J.K., et al., 2000. The use of shaded fuelbreaks in landscape fire management. For. Ecol. Manage. 127 (1), 55–66.

Allen, R.G., Trezza, R., Tasumi, M., 2006. Analytical integrated functions for daily solar radiation on slopes. Agric. For. Meteorol. 139 (1–2), 55–73.

Anderson, M.C., 1964. Studies of the woodland light climate: I. The photographic computation of light conditions. J. Ecol. 52 (1), 27–41.

Baldocchi, D., Collineau, S., 1994. The Physical Nature of Solar Radiation in Heterogeneous Canopies: Spatial and Temporal Attributes. In: Caldwell, M.M., Pearcy, R.W. (Eds.), Exploitation of Environmental Heterogeneity by Plants. Academic Press, New York, pp. 21–71.

Baret, F., Weiss, M., 2004. Can-Eye: Processing Digital Photographs for Canopy Structure Characterization. CAN EYE Tutorial Document, Avignon, France.

Berry, G., Rothwell, R., 1992. Snow ablation in small forest openings in southwest Alberta. Can. J. For. Res. 22 (9), 1326–1331.

Canham, C.D., 1988. An index for understory light levels in and around canopy gaps. Ecology 69 (5), 1634–1638.

Canham, C.D., et al., 1990. Light regimes beneath closed canopies and tree-fall gaps in temperate and tropical forests. Can. J. For. Res. 20 (5), 620–631.

Clark, D.A., Clark, D.B., 1992. Life history diversity of canopy and emergent trees in a neotropical rain forest. Ecol. Monogr. 62 (3), 315–344.

DeBeer, C., Pomeroy, J., 2010. Simulation of the snowmelt runoff contributing area in a small alpine basin. Hydrol. Earth Syst. Sci. Discuss. 7 (1), 971–1003.

Denslow, J.S., 1980. Gap partitioning among tropical rainforest trees. Biotropica 12 (2), 47–55.

Ellis, C., Pomeroy, J., Link, T., 2013. Modeling increases in snowmelt yield and desynchronization resulting from forest gap-thinning treatments in a northern mountain headwater basin. Water Resour. Res. 49 (2), 936–949.

Ellis, C.R., Pomeroy, J.W., 2007. Estimating sub-canopy shortwave irradiance to melting snow on forested slopes. Hydrol. Processes 21 (19), 2581–2593.

Essery, R., Pomeroy, J., 2004. Implications of spatial distributions of snow mass and melt rate for snow-cover depletion: theoretical considerations. Ann. Glaciol. 38 (1), 261–265.

Essery, R., Pomeroy, J., Ellis, C., Link, T., 2008. Modelling longwave radiation to snow beneath forest canopies using hemispherical photography or linear regression. Hydrol. Processes 22 (15), 2788–2800.

Essery, R.L., Pomeroy, J.W., Parviainen, J., Storck, P., 2003. Sublimation of snow from coniferous forests in a climate model. J. Clim. 16, 1855–1864.

Faria, D.A., Pomeroy, J.W., Essery, R.L.H., 2000. Effect of covariance between ablation and snow water equivalent on depletion of snow-covered area in a forest. Hydrol. Processes 14 (15), 2683–2695.

Finney, M.A., 2001. Design of regular landscape fuel treatment patterns for modifying fire growth and behavior. For. Sci. 47 (2), 219–228.

Golding, D.L., Swanson, R.H., 1978. Snow accumulation and melt in small forest openings in Alberta. Can. J. For. Res. 8 (4), 380–388.

Golding, D.L., Swanson, R.H., 1986. Snow distribution patterns in clearings and adjacent forest. Water Resour. Res. 22 (13), 1931–1940.

Gower, S.T., Norman, J.M., 1991. Rapid estimation of leaf area index in conifer and broad-leaf plantations. Ecology 72 (5), 1896–1900.

Gray, A.N., Spies, T.A., 1996. Gap size, within-gap position and canopy structure effects on conifer seedling establishment. J. Ecol. 84 (5), 635–645.

Gray, A.N., Spies, T.A., Easter, M.J., 2002. Microclimatic and soil moisture responses to gap formation in coastal Douglas-fir forests. Can. J. For. Res. 32 (2), 332–343.

Hopkinson, C., Pomeroy, J., Debeer, C., Ellis, C., Anderson, A., 2012. Relationships between Snowpack Depth and Primary LiDAR Point Cloud Derivatives in a Mountainous Environment. IAHS–AISH Publication, Jackson, Wyoming, USA, pp. 354–358.

Kirby, C.L., Ogilvy, R.T., 1969. The Forest of Marmot Creek Watershed Research Basin. Canadian Forest Service, Northern Forest Research Centre, Edmonton.

Lawler, R.R., Link, T.E., 2011. Quantification of incoming all-wave radiation in discontinuous forest canopies with application to snowmelt prediction. Hydrol. Processes 25 (21), 3322–3331.

Lieberman, M., Lieberman, D., Peralta, R., 1989. Forests are not just Swiss cheese: canopy stereogeometry of non-gaps in tropical forests. Ecology 70 (3), 550–552.

Lundquist, J.D., Dickerson-Lange, S.E., Lutz, J.A., Cristea, N.C., 2013. Lower forest density enhances snow retention in regions with warmer winters: a global framework developed from plot-scale observations and modeling. Water Resour. Res. 49 (10), 6356–6370.

MacFarlane, A., 1999. Revegetation of Wellsites and Seismic Lines in the Boreal Forest. Alberta Centre for Boreal Studies.

Male, D.H., Gray, D.M., 1981. Snowcover Ablation and Runoff. In: Gray, D.M., Male, D.H. (Eds.), Handbook of Snow. Pergamon, Ont., Toronto, pp. 360–436.

Marks, D., Dozier, J., Davis, R.E., 1992. Climate and energy exchange at the snow surface in the Alpine region of the Sierra Nevada: 1. Meteorological measurements and monitoring. Water Resour. Res. 28 (11), 3029–3042.

Marsh, C.B., Pomeroy, J.W., Spiteri, R.J., 2012. Implications of mountain shading on calculating energy for snowmelt using unstructured triangular meshes. Hydrol. Processes 26 (12), 1767–1778.

Meromy, L., Molotch, N.P., Link, T.E., Fassnacht, S.R., Rice, R., 2013. Subgrid variability of snow water equivalent at operational snow stations in the western USA. Hydrol. Processes 27 (17), 2383–2400.

Miller, D.H., 1959. Transmission of insolation through pine forest canopy, as it affects the melting of snow Mitteilungen der Schweizerischen Anstalt Fur das forstliche Versuchswesen. Versuchsw. Mitt 35, 35–79.

Monsi, M., Saeki, T., 1953. Über den Lichtfaktor in den Pflanzengesellschaften und seine Bedeutung für die Stoffproduktion. Jpn. J. Bot. 14, 22–52.

Monteith, J., 1972. Solar radiation and productivity in tropical ecosystems. J. Appl. Ecol. 9 (3), 747–766.

Musselman, K.N., Margulis, S.A., Molotch, N.P., 2013. Estimation of solar direct beam transmittance of conifer canopies from airborne LiDAR. Remote Sens. Environ. 136, 402–415.

Musselman, K.N., Molotch, N.P., Margulis, S.A., Lehning, M., Gustafsson, D., 2012. Improved snowmelt simulations with a canopy model forced with photo-derived direct beam canopy transmissivity. Water Resour. Res. 48 (10), http://dx.doi.org/10.1029/2012WR012285, W10509.

Ni, W., Li, X., Woodcock, C.E., Caetano, M.R., Strahler, A.H., 1999. An analytical hybrid GORT model for bidirectional reflectance over discontinuous plant canopies. IEEE Trans. Geosci. Remote Sens. 37 (2), 987–999.

Ni, W., Li, X., Woodcock, C.E., Roujean, J.-L., Davis, R.E., 1997. Transmission of solar radiation in boreal conifer forests: measurements and models. J. Geophys. Res. 102 (D24), 29555–29566.

Nicotra, A.B., Chazdon, R.L., Iriarte, S.V., 1999. Spatial heterogeneity of light and woody seedling regeneration in tropical wet forests. Ecology 80 (6), 1908–1926.

Nijssen, B., Lettenmaier, D.P., 1999. A simplified approach for predicting shortwave radiation transfer through boreal forest canopies. J. Geophys. Res. 104 (D22), 27859–27868.

Northrup, J.M., Wittemyer, G., 2013. Characterising the impacts of emerging energy development on wildlife, with an eye towards mitigation. Ecol. Lett. 16 (1), 112–125.

Peng, S., Zhao, C., Xu, Z., 2014. Modeling spatiotemporal patterns of understory light intensity using airborne laser scanner (LiDAR). ISPRS J. Photogramm. Remote Sens. 97, 195–203.

Pickell, P.D., Andison, D.W., Coops, N.C., 2013. Characterizations of anthropogenic disturbance patterns in the mixedwood boreal forest of Alberta, Canada. For. Ecol. Manage. 304, 243–253.

Pomeroy, J., et al., 2008. Spatial variability of shortwave irradiance for snowmelt in forests. J. Hydrometeorol. 9 (6), 1482–1490.

Pomeroy, J.W., Dion, K., 1996. Winter radiation extinction and reflection in a boreal pine canopy: measurements and modelling. Hydrol. Processes 10 (12), 1591–1608.

Pomeroy, J.W., et al., 1998. An evaluation of snow accumulation and ablation processes for land surface modelling. Hydrol. Processes 12 (15), 2339–2367.

Pomeroy, J.W., Hanson, S., Faria, D., 2001. Small-scale Variation in Snowmelt Energy in a Boreal Forest: an Additional Factor Controlling Depletion of Snow Cover? Proceedings of the Eastern Snow Conference 58, 85–96.

Pomeroy, J.W., et al., 2009. The impact of coniferous forest temperature on incoming longwave radiation to melting snow. Hydrol. Processes 23 (17), 2513–2525.

Reda, I., Andreas, A., 2004. Solar position algorithm for solar radiation applications. Sol. Energy 76 (5), 577–589.

Reifsnyder, W.E., Furnival, G.M., Horowitz, J.L., 1971. Spatial and temporal distribution of solar radiation beneath forest canopies. Agric. Meteorol. 9, 21–37.

Rich, P., Dubayah, R., Hetrick, W., Saving, S., 1994. Using Viewshed Models to Calculate Intercepted Solar Radiation: Applications in Ecology. American Society for Photogrammetry and Remote Sensing Technical Papers.

Runkle, J.R., 1981. Gap regeneration in some old-growth forests of the eastern United States. Ecology 62 (4), 1041–1051.

Runkle, J.R., 1982. Patterns of disturbance in some old-growth mesic forests of eastern North America. Ecology 63 (5), 1533–1546.

Satterlund, D.R., 1983. Forest shadows: how much shelter in a shelterwood? For. Ecol. Manage. 5 (1), 27–37.

Seyednasrollah, B., Kumar, M., 2014. Net radiation in a snow-covered discontinuous forest gap for a range of gap sizes and topographic configurations. J. Geophys. Res. Atmos. 119 (17), 10323–10342.

Seyednasrollah, B., Kumar, M., Link, T.E., 2013. On the role of vegetation density on net snow cover radiation at the forest floor. J. Geophys. Res. Atmos. 118 (15), 8359–8374.

Smith, N., Chen, J., Black, T., 1993. Effects of clumping on estimates of stand leaf area index using the LI-COR LAI-2000. Can. J. For. Res. 23 (9), 1940–1943.

Spies, T.A., Franklin, J.F., 1989. Gap characteristics and vegetation response in coniferous forests of the Pacific Northwest. Ecology 70 (3), 543–545.

Thompson, S.E., Harman, C.J., Troch, P.A., Brooks, P.D., Sivapalan, M., 2011. Spatial scale dependence of ecohydrologically mediated water balance partitioning: a synthesis framework for catchment ecohydrology. Water Resour. Res. 47 (10).

Troendle, C.A., 1983. The potential for water yield augmentation from forest management in the Rocky Mountain region. JAWRA J. Am. Water Res. Assoc. 19 (3), 359–373.

Western, A.W., Grayson, R.B., Blöschl, G., Willgoose, G.R., McMahon, T.A., 1999. Observed spatial organization of soil moisture and its relation to terrain indices. Water Resour. Res. 35 (3), 797–810.